

# Improved design of Savonius rotor for green energy production from moving Singapore metropolitan rapid transit train inside tunnel

Praveen Laws<sup>1</sup> , Rajagopal V Bethi<sup>1</sup>, Pankaj Kumar<sup>2</sup> and Santanu Mitra<sup>1</sup>

Proc IMechE Part C:  
J Mechanical Engineering Science  
0(0) 1–16  
© IMechE 2018  
Reprints and permissions:  
sagepub.co.uk/journalsPermissions.nav  
DOI: 10.1177/0954406218784620  
journals.sagepub.com/home/pic



## Abstract

Nonrenewable fossil fuels are finite resources that will ultimately deplete in near future. Nature sheds colossal amount of renewable wind energy but humans harvest a morsel. Taking this into account a numerical study is proposed on wind energy harvesting from a speeding subway train. Subways trains generate a remarkable gust of wind that can be transferred to useful electrical energy on daily basis. To this aim, a numerical analysis is modeled by placing Savonius wind turbine in a subway tunnel to crop the wind energy produced from the speeding train. The passage of train in the tunnel generates very high velocity slipstreams along the length of the tunnel. The slipstream phenomena develop a boundary layer regime that will be absorbed by the Savonius wind turbine to self-start and generate power. In the present study, a two-dimensional numerical simulation with modified turbine blade design is carried out using open source tool OpenFOAM<sup>®</sup> with PimpleDyMFoam solver coupled with six degrees of freedom mesh motion solver sixDoFRigidBodyMotion and  $k-\varepsilon$  turbulence modeling, to measure the amount of torque predicted by the rotor from the gust of wind produced by the speeding train in the tunnel. Being a self-start turbine with no yaw mechanism required the turbine collects air from any direction and converts it into useful power.

## Keywords

Renewable energy, Savonius wind turbine, subway train, tunnel, OpenFOAM<sup>®</sup>

Date received: 6 February 2018; accepted: 24 May 2018

## Introduction

Fossil fuels are the main cause of global warming; these fuels when burnt emit harmful gases such as sulfur dioxide and carbon dioxide. Fossil fuels will deplete soon as they are a finite nonrenewable resource. Numerous researches are focused on effective concepts to harvest the freely available renewable energy. The major renewable resources available are the wind energy, solar energy, biomass energy, geothermal energy, and hydropower. Among all these resources the most generally available and world's second fastest-growing resource is the wind energy. A newfangled concept is proposed to harvest wind energy conceived by a speeding train in a tunnel with optimized Savonius turbine blades. Movement of train in a tunnel alters the pressure and air velocity between the train–tunnel annulus. A moving train in tunnel will deflect the air and make it flow parallel to the length of the train–tunnel.<sup>1</sup> The flow around the train surface builds up aerodynamic forces that are

directly proportional to the train speed, train dimension, and tunnel length. These unsteady aerodynamic forces were due to (i) the pressure pulse effect as discussed above and (ii) train-induced airflow or slipstream formation. An abrupt change in pressure is predicted as the induced airflow by the train interacts with the tunnel wall. The train-induced airflow forms a boundary layer along the train length and wake vortices behind the train. Due to viscous effect, the air around the train will be dragged along the train length with the speed of the train.<sup>2</sup> These pressure variations initiate a wind discomfort of around 5 m/s

<sup>1</sup>Department of Mechanical Engineering, Shiv Nadar University, Tehsil Dadri, Uttar Pradesh, India

<sup>2</sup>Department of Fluid Dynamics (FD), Institute of High Performance Computing, A\*STAR, Singapore

### Corresponding author:

Santanu Mitra, Department of Mechanical Engineering, School of Engineering, Tehsil Dadri, Uttar Pradesh 201314, India.  
Email: Santanu.Mitra@snu.edu.in

that will be experienced on the platform. While at the end of the tunnel forms a huge gust of wind and air buffeting which might lead to wind danger of about 12 m/s when the train travels at 140 km/h. Similarly speeding vehicles in road drag out huge gust of air, so setting up wind turbines in the side or in the middle of roadways helps to reap wind flow. Turbines fixed in the median were able to capture airflow from both the directions. The turbines are aligned so that the wakes formed at the end of the turbine will flow in the vehicle direction reducing the resistance against the moving body and increasing the mileage.<sup>3</sup> Taiming Chen<sup>4</sup> filed a patent on extracting wind power by providing with two-way airflow duct along the traffic with an inlet facing opposite direction of the road, outlet that faces toward the direction of the road, and middle opening for each provides the working fluid for the installed turbines.

Designer Ryu Chan, Sinhyung and Hong Sun<sup>5</sup> proposed a new concept of fixing small-scaled wind turbines on the walls of the tunnel for generating clean electricity. Design engineers Qian and Alessandro designed a T-box concept, which can be installed in railway or subway tunnel tracks. The turbines were placed inside a cylindrical grill housing so that the turbine blades rotate with its central axis. The turbines harvest wind energy from the speeding train that travels over the railway track. The major setback in the design is that speeding train deposits dust, debris, grease, and oil waste on the surface of the cylindrical grill housing, thus blocking air causing maintenance issue.<sup>6</sup> Wind energy is available 70% of the time but the available wind strength is not fine enough to rotate most of the turbines that leads to poor power production. Power attainable is directly proportional to the cube of wind velocity. Khadka demonstrated a possible way to increase the wind flow around the turbine is by constructing a venture tube setup. The channel setup helps for a constant steady flow of air to the turbine and increases its efficiency as the venture tube reduces the pressure and increases the flow velocity to the turbine, resulting in increased power production.<sup>7</sup> For improved rotor performance modifications required on the existing conventional Savonius turbine blades, one such design is the combined end blades to form a circular concave model. The construction of the blades remains simple. The combined blades will increase the power coefficient of the rotor to about 11% of the conventional rotor and stable with tip speed ratio. As the torque generated in the concave side is higher than the torque in the convex side, this reduction in the negative torque in convex side leads to improve the power coefficient. The construction of the combined blades remains simple as that of the conventional type rotor.<sup>8</sup> The velocity of the wind raises up to 1.5 times to that of the train when it travels inside a tunnel and also positioning of the turbine at an ideal point is the main area of

consideration. Placing the turbine at one car length distance away from the tunnel exit allows the turbine to absorb steady wind flow with higher velocity. Instead, if the turbine is placed closer to the tunnel exit leads to poor wind velocity with the unsteady flow.<sup>9</sup> The aim of this present study is to harness the wind energy form a speeding train in a tunnel. Slipstreams generate huge fluctuating force of gust wind near the trackside. The intensity of these slipstreams is strengthened near the boundary layer region that occurs along the length of the train. Therefore, the main objective is to predict the practical application of harvesting wind energy from this adverse gradient flow. The simulation is proposed in such a way by placing a self-start Savonius turbine in the region of interest and considering the train is moving continuously in a closed-loop tunnel. Finally, the amount of torque and power extracted by the turbine from the gusting wind is measured for different train speed.

## Mathematical formulation

### Governing equations

The entire simulation in the present study is demonstrated using dimensionless Reynolds number, which is defined as

$$Re = \frac{DU_{\infty}}{\nu} \quad (1)$$

where  $\nu$  is the kinematic viscosity,  $D$  is the diameter of the rotor, and  $U_{\infty}$  is the free stream wind velocity.

The flow is governed by incompressible Navier–Stokes equations described as

$$\frac{\partial \mathbf{u}}{\partial t} + \nabla \cdot (\mathbf{u}\mathbf{u}) = -\nabla p + \nu \Delta \mathbf{u} \quad (2)$$

The fluid flow incompressibility is defined by the continuity equation

$$\nabla \cdot \mathbf{u} = 0 \quad (3)$$

For turbulent flow, the field variables start to fluctuate and become random in both time and space, therefore equations (2) and (3) are time averaged to form Reynolds-averaged Navier–Stokes equation

$$\frac{\partial \bar{\mathbf{u}}}{\partial t} + \nabla \cdot (\bar{\mathbf{u}}\bar{\mathbf{u}}) - \nabla \cdot (\nu \nabla \bar{\mathbf{u}}) = -\nabla \bar{p} + \Delta \cdot (\overline{\mathbf{u}'\mathbf{u}'}) \quad (4)$$

$$\nabla \cdot \bar{\mathbf{u}} = 0 \quad (5)$$

### Turbulence modeling

The unknown term  $(\overline{\mathbf{u}'\mathbf{u}'})$  in equation (4) is modeled using the Standard  $k-\epsilon$  model, widely used workhorse

model for flow simulation around turbine blades and slipstream phenomena around the train.<sup>10</sup> The two-equation  $k$ - $\epsilon$  turbulence model solves for turbulence kinetic energy ( $k$ ) and rate of dissipation ( $\epsilon$ ) of turbulence kinetic energy.

Turbulence kinetic energy

$$\frac{\partial k}{\partial t} + \nabla \cdot (\bar{u}k) - \nabla \cdot [(v)\nabla k] = v_t \left[ \frac{1}{2} (\nabla \bar{u} + \nabla \bar{u}^T) \right]^2 - \epsilon \quad (6)$$

Dissipation rate

$$\begin{aligned} \frac{\partial \epsilon}{\partial t} + \nabla \cdot (\bar{u}\epsilon) - \nabla \cdot [(v)\nabla \epsilon] \\ = C_1 \frac{\epsilon}{k} v_t \left[ \frac{1}{2} (\nabla \bar{u} + \nabla \bar{u}^T) \right]^2 - C_2 \frac{\epsilon^2}{k} \end{aligned} \quad (7)$$

### Train dynamics

The aerodynamic coefficients propagating along the surface of the speeding train is represented by

Lateral lift coefficient

$$C_{L(train)} = \left( \frac{L_{train}}{\frac{1}{2} \rho A V_\infty^2} \right) \quad (8)$$

Longitudinal drag coefficient (side force)

$$C_{D(train)} = \left( \frac{D_{train}}{\frac{1}{2} \rho A V_\infty^2} \right) \quad (9)$$

From both the equations, the term  $\frac{1}{2} \rho V_\infty^2$  denotes the dynamic pressure of air,  $A$  is the reference area of the train,  $L_{train}$  is the lift force on the train,  $D_{train}$  is the drag force on train, and  $V_\infty$  is the velocity of train.

### Rotor dynamics

The coefficient of dynamic torque ( $C_m$ ) and coefficient of power ( $C_p$ ) obtained by the Savonius rotor is represented by

$$C_m = \left( \frac{M}{0.5 \rho A R U_\infty^2} \right) \quad (10)$$

$$C_p = \left( \frac{P}{0.5 \rho A U_\infty^3} \right) \quad (11)$$

where  $A$  is the area of the rotor,  $R$  is the rotor radius,  $P$  is the power generated by the rotor,  $M$  is the rotor moment, and  $\rho$  is the air density

The rotor downwind force ( $C_D$ ) and side force ( $C_L$ ) were expressed as the dimensionless aerodynamic coefficients

$$C_D = \left( \frac{D}{0.5 \rho A U_\infty^2} \right) \quad (12)$$

$$C_L = \left( \frac{L}{0.5 \rho A U_\infty^2} \right) \quad (13)$$

where  $D$  is the rotor drag force (N) and  $L$  is the rotor lift force (N).

## Geometrical characteristics of control volume

### Rotor geometry and design

The construction of the rotor is simple with two semi-circular blades of diameter ( $d$ ), overall rotor diameter ( $D$ ) of the turbine, angular rotation of the rotor ( $\omega$ ), and azimuthal angle of the blades ( $\theta$ ). The both end combined blades and one end combined blades are the modification of the conventional Savonius rotor blades as shown in Figure 1. The study has been performed in such a way that a performance comparison is made with respective different train speeds.

### Computation domain and boundary conditions

The proposed two-dimensional model of the train design is based on the dimensions of Singapore metropolitan rapid transit (SMRT) corporation circle line. The train and the turbine were modeled using Gmsh 3.0.2. The aerodynamic performance of the blades is considered avoiding the shaft and other components of the rotor to minimize computation time. The geometry is composed of two domains: rotating circular inner domain and stationary rectangular outer domain. The rectangular outer domain is of 10 m  $\times$  2.9 m mount the train of width 1.6 m and length of 5 m, dimensions of the train are selected from the scaled model of Alstom Metropolis C830C<sup>11</sup> were discussed in Figure 2 and Table 1. The rotating domain mounts the turbine of diameter 0.5 m that rotates with an angular velocity,  $\omega$ . The domain dimensions allow the train to generate fully developed drag flow to the turbine. The blockage ratio is similar to that of the blockage between the train (Alstom Metropolis C830C) and the tunnel (SMRT circle line) which is about 0.54 and the blockage ratio by placing the turbine between the train and tunnel will be about 0.63. A continuous circulation of air in the domain is considered and assumption is made with the movement of the train in the domain as closed-loop structure which agnate dynamic similarity in a wind tunnel testing. The boundary condition is composed of pressure outlet on the left, velocity inlet on the right, top wall, bottom symmetry plane, train walls, and turbine

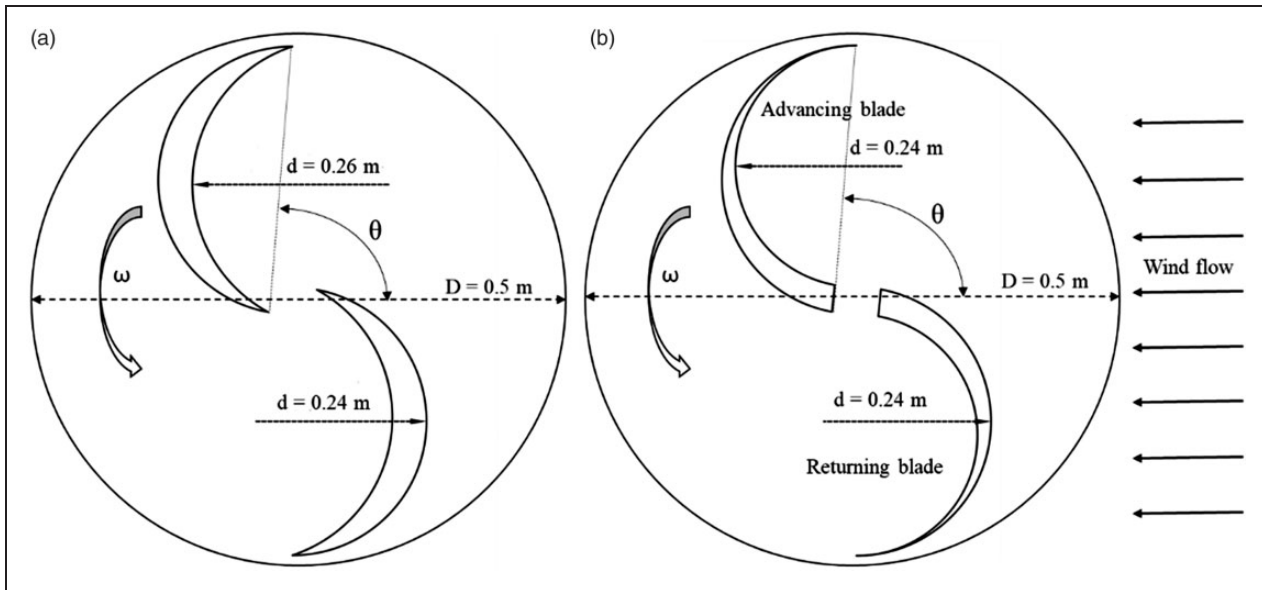


Figure 1. Rotor models: (a) both end combined blade and (b) one end combined blade.

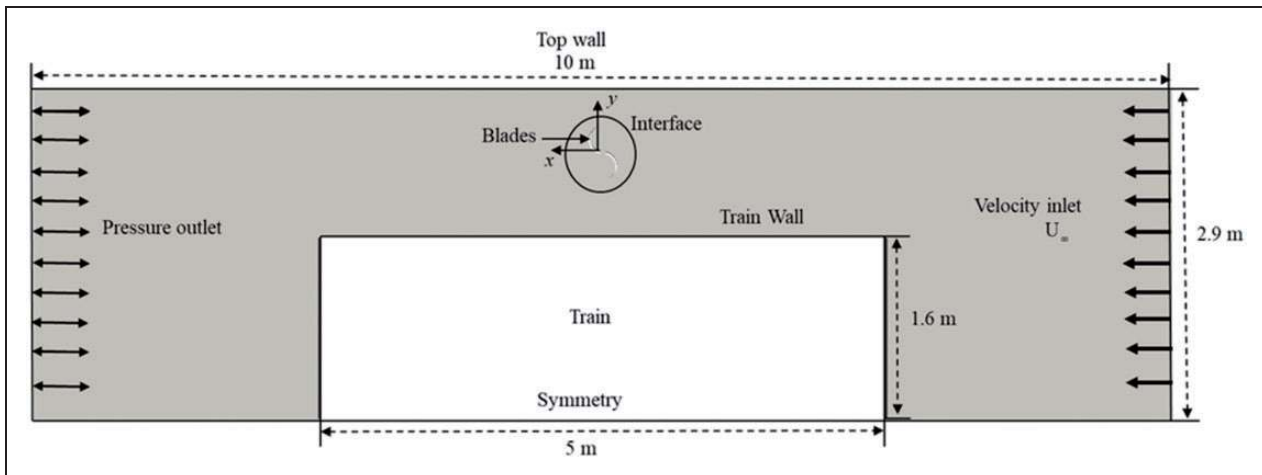


Figure 2. Schematic and boundary conditions of the proposed model.

Table 1. Model parameters for the simulation.

| Parameters                | Dimensions   |
|---------------------------|--|
| Length of the train (m)   | 5  |
| Width of the train (m)    | 1.6  |
| Length of the tunnel (m)  | 10   |
| Width of the tunnel (m)   | 2.9  |
| Train speed (m/s)         | 6, 12, 18<br>( $Re = 2.03 \times 10^5$ ,<br>$Re = 4.06 \times 10^5$ ,<br>$Re = 6.09 \times 10^5$ ) |
| Diameter of the rotor (m) | 0.5  |

walls. Symmetry condition is imposed so that it maintains the stability of the simulation and allows the solver to consider the domain further large.<sup>12</sup> For pressure, zero gradient boundary condition is

imposed on the train walls, top wall, rotor, inlet and fixed value constraint is applied to the outlet. In case of velocity file, moving wall velocity is set on the rotor walls. The rotation of the turbine is achieved using arbitrary mesh interface (AMI) that allows contribution from overlapping faces between the stationary and rotating domain. The discussed technique is more suitable for rotating geometries that require separate mesh for the fixed and rotating domain. Both the interfaces are coupled using cyclic AMI boundary condition. While sliding each other the patch faces transfer contribution between the faces, the sum of contributions between intersecting areas should equal to 1.<sup>13</sup>

### Mesh characteristics

Open source utility Gmsh 3.0.2 is used to generate mesh. The first node above the wall is set based

on the given equation

$$y^+ = \frac{y}{\delta} \sqrt{\frac{\tau_w}{\rho}} \quad (14)$$

$$\tau_w = \mu \left( \frac{\partial u}{\partial y} \right) \quad (15)$$

where  $\tau_w$  is the wall shear stress and  $\Delta y$  is the thickness of the first mesh layer. Calculated dimensionless wall distance of 149 is applied in the study.

Unstructured hexahedral mesh of about 30,000 elements with highly refined boundary layer grids around the area detects the train walls and the turbine blades as shown in Figure 3. The convergence of the current problem is monitored using the magnitude of residual values obtained from the simulation, which is one of the most fundamental solution convergence measures. Lesser the residual value proves that the numerical solutions are more accurate. In this present research, the RMS residual levels of 1E-6 are set which defines that the solution is tightly converged. In addition, the Courant number for the entire simulation is kept below 0.1 to sustain stability and accuracy. At the inlet, a turbulence intensity of 0.03% is set, while the maximum nonorthogonality of the grid is about 80 and maximum skewness of the cells is about 0.86.

## Methodology

Standard OpenFOAM® RANS solver pimpleDyMFoam has been selected for this investigation, a transient solver can adopt dynamic mesh with large time step for both laminar and turbulent flow. An incompressible flow solver for Newtonian fluids and turbulent flows for moving mesh with a combination of PISO-SIMPLE algorithm is called PIMPLE algorithm. The pressure-velocity coupling is done by PIMPLE algorithm which solves the momentum equation to find the velocity field  $U^*$  from the guessed pressure  $p^*$  and later the pressure and velocity field are corrected explicitly. The iteration goes on until it reaches the maximum else it takes a new iteration with the same time step.<sup>14</sup> The rotation and morphing of grids were performed in the analysis using the dynamic MeshDict dictionary that supports SixDoFRigidBodyMotion utility. SixDoFRigidBodyMotion solver helps to mimic the rotation of the rotor to counter the shear force and pressure generated by the inflow air. The resultant force and moment acting on the rotor then solves the governing equations to find the new position of the turbine blades.

A mass of 5 kg and moment of inertia  $I = 0.1 \text{ kgm}^2$  were set in the dynamicMeshDict dictionary for the rotor. The rotor motion is restricted only to Z-axis; this allows the rotor to rotate in a constrained axis

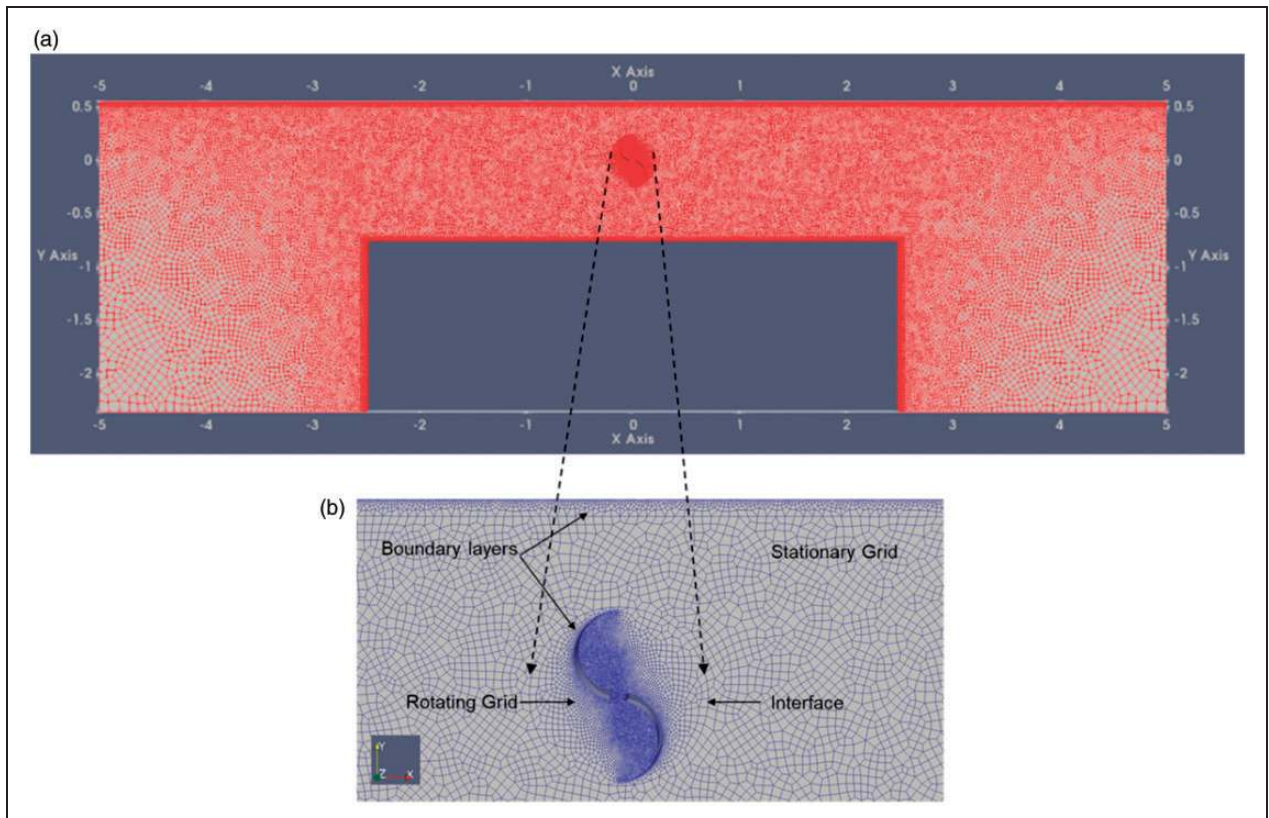


**Figure 3.** (a) Overview of the mesh around domain and (b) blade.

with one degree of freedom in rotation.<sup>15</sup> Kinematic viscosity,  $\nu$  of air is set as  $1.5 \times 10^{-5} \text{ m}^2/\text{s}$ . The time derivatives are discretized using the Euler scheme which is first-order implicit suitable for transient simulations. The gradient of pressure and velocity is discretized using the Gauss linear scheme which specifies the Gaussian interpolation of values from cell center to face center, while the divergence term, namely advection of velocity, advection of epsilon, and turbulent kinetic energy were discretized with Gauss upwind linear scheme which is of second order and upwind biased. The Laplacian terms are discretized using Gauss linear corrected which poses numerical behavior of second order and unbounded. The maximum Courant number for all the simulation is fixed to 0.1, with a time step of  $\Delta t = 1\text{E-}07 \text{ s}$  and 4s is specified for the end time.

## Result and discussion

The initial numerical study is focused on the region around the train surface primitively to study the regions of interest in the thickening boundary layer to harness the wind. Therefore, two analyses were performed to find the aerodynamic flow field around the train with a dynamic train and a static train. The dynamic simulation is performed using OpenFOAM<sup>®</sup> solver pimpleDyMFOam and static simulation is done using pimpleFoam solver. The magnitude of velocity field for both the simulations was compared and discussed.

### Dynamic simulation

Dynamic motion of the train is simulated using pimpleDyMFOam solver with  $k-\epsilon$  turbulence modeling and a moving wall velocity of 18 m/s. The velocity magnitude along the surface of the train is monitored throughout the simulation to predict the strength of slipstream boundary layer regime. The movement of the train in tunnel predicts a localized peak pressure near the boundary layer regime and drop in pressure near the tail as shown in Figure 4. The velocity magnitude plot of the moving train with respect to time gives a clear picture of how the velocity flow field behaves around the train surface with strong shear stress as shown in Figure 5(a) to (c). The velocity of

the moving train is directly proportional to the shear stress formation along the train surface that in turn increases the slipstream velocity. The forward motion of the train in the tunnel makes a frontal impact with the induced air and pushes it to flow in the opposite direction. The frontal impact reduces the air velocity and increases the slipstream velocity around the train surface with high stagnation pressure.<sup>16</sup> The formation of boundary layer and increased air velocity is the main region of interest from which the useful power is harvested.

### Static analysis

The static analysis is simulated using pimpleFoam solver. In the static analysis, the train is kept stationary and an inlet velocity of 18 m/s is imposed. The velocity contour plot of the static simulation as shown in Figure 5(d) predicts an increased flow field in the region of interest along the length of the train. The inlet flow makes a frontal impact with the bluff body and diverges the air toward the train length. The formation of slipstream boundary layer regime between continuously moving train with constant velocity and a fully developed flow around stationary train is taken in to account. The velocity magnitude plot for both the static and dynamic simulation of train shows a similar trend between the tunnel wall and the train surface. The fully developed velocity flow field after the train started to move with a constant speed in the dynamic simulation is compared against the static case. Worst-case scenario of freight train structure is considered which contributes strongest slipstream in the boundary layer regime. The aim is to extract wind energy from a fully developed high sheared flow. In order to reduce computational time, resource, and the study sample, stationary train is selected for the study based on the principle followed in the wind tunnel air dynamic test. Moreover, the performance of the turbine near the head and tail section of the train is not taken into account as their influence on the turbine is for very small periods and only the coach length is considered.

In addition, the downstream distance considered for the study is consistent and sufficient for the entire simulation as the measured outlet pressure for

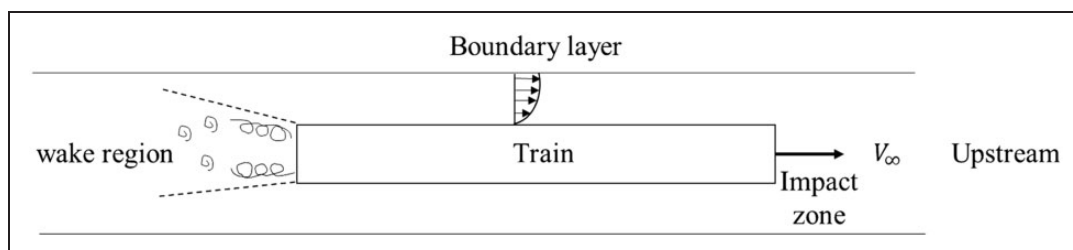
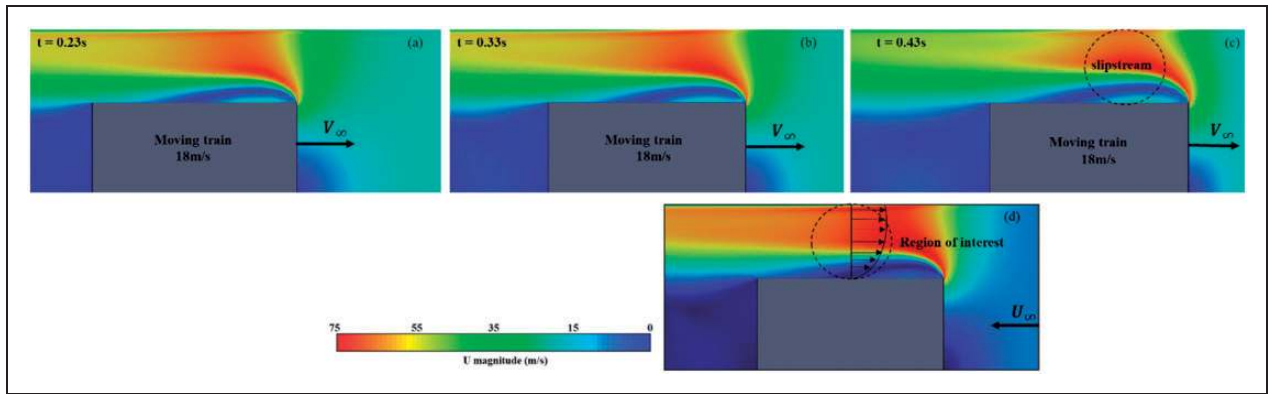
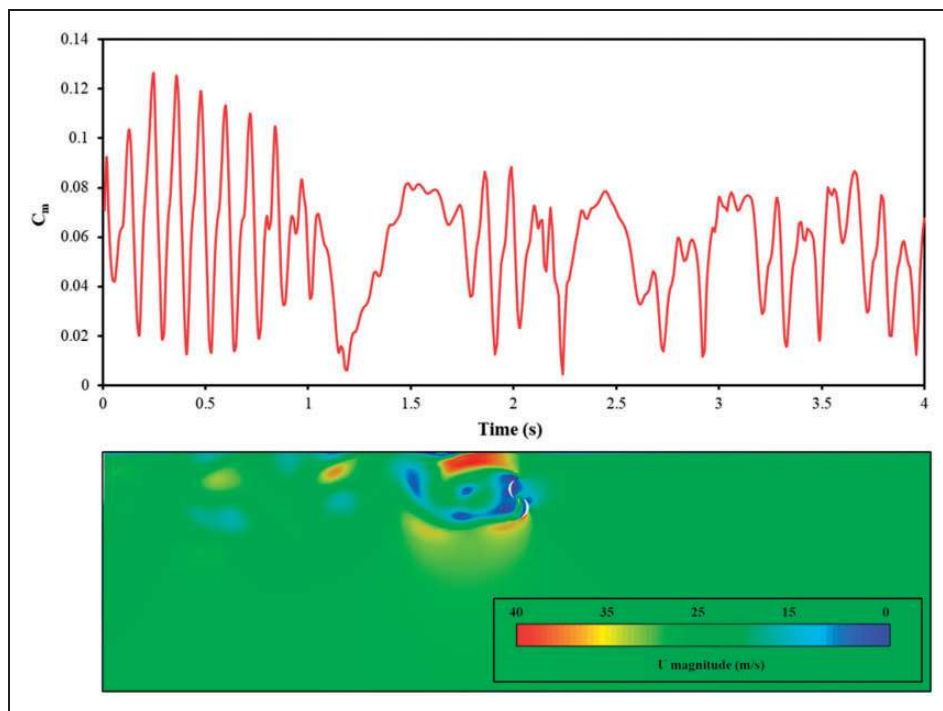


Figure 4. Slipstream regions along the train surface.



**Figure 5.** (a) Velocity magnitude plot of moving train at  $t = 0.23$  s, (b)  $t = 0.33$  s, (c)  $t = 0.43$  s, and (d) stationary train velocity magnitude.



**Figure 6.** Predicted torque coefficient,  $C_m$  and velocity field in the domain without train at  $U_\infty = 18$  m/s.

both the static and dynamic simulation of train falls similar with no significant variation.

### Rotor performance

The performance of the rotor is measured based on the natural circulation of air in the tunnel without the considering the train. The change in aerodynamic coefficients on the rotor blades operates the turbine and these pressure coefficients vary with the change in azimuthal angle of the blades. Therefore, the stable performance of the turbine without the train is tested against a uniform flow,  $U_\infty = 18$  m/s. During acceleration phase, the graph shows instability due to start–stop phase and the rotor predicts peak torque coefficient,  $C_m$  around 0.126 and after  $t = 1.28$  s the values become cyclic announcing the

equilibrium. The stabilized solution predicts an averaged torque coefficient,  $C_m$  of 0.06 and an averaged power coefficient,  $C_p$  of about 0.033. Thus, the considered parameters and boundary conditions are suitable for predicting torque and power coefficient from the moving train. The predicted velocity field as shown in Figure 6 and torque coefficient plot show a good argument in terms of natural circulation of air in the tunnel.

### Residual convergence

The convergence of the current simulation is monitored by reviewing the residual plot. The residual values were calculated from each grid point stating how the governing equation for the numerical simulation is satisfied. Therefore, for both the two different

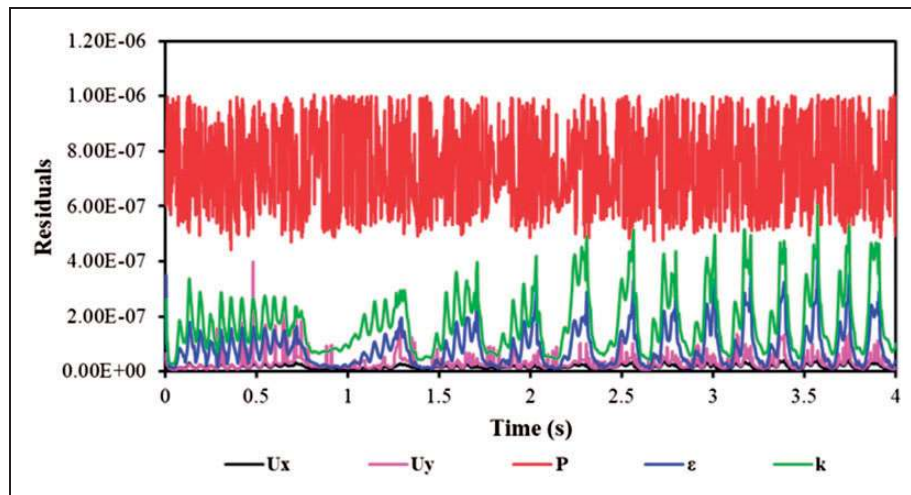


**Figure 7.** Residual convergence of the rotor at 18 m/s train speed.

rotor simulations the convergence criteria are achieved by the fundamental solution convergence measure of the RMS residual levels. The RMS residual levels for the simulation are set to  $1E-6$  for continuity, momentum, and turbulence properties with two sets of iterations for one time step which defines the solution is tightly converged.<sup>17</sup> Hence, the simulation is modeled that all the scaled residual values had to fall below  $1E-6$  to obtain a tightly converged and accurate solution as shown in Figure 7. Once the convergence is met, OpenFOAM® addresses the pressure, viscous, and moment forces. The plot displays a sinusoidal wave pattern in Figure 7 that describes rotational motion; the steadiness of the system depends mainly on the turbulence properties, which remains steady with wind velocity.

**Rotor with one end combined blade.** Wind power extraction using Savonius wind turbine is performed with three different train speeds 6 m/s (21.6 km/h), 12 m/s (43.2 km/h), and 18 m/s (65 km/h), respectively. The performance of the considered blade models is compared based on the amount of torque coefficient and power coefficient predicted by the rotor blades. The rotor is placed in the midsection of the railway tunnel assuming a continuous motion of train in the tunnel. This particular assumption is based on closed-loop wind tunnel that constantly recirculates the air accomplishing the wind velocity along the length of the tunnel proportional to the train speed,  $V_{\infty}$ . The total length of SMRT train is 70.1 m; if the train travels with a minimum speed of 6 m/s between stations then the time taken by the train to pass by the rotor is  $t = 12$  s.<sup>10</sup> The calculated time taken by the train to go past the rotor is considered as the observation time to predict the power generated by the rotor. This observation time varies with different train speeds. In addition, for simulation point of view the length of the train is considered as 5 m. The air speed inside the tunnel due to train movement relies on the speed of

the train. The study is mainly focused on the amount of energy extracted from a train that passes through a drag-based Savonius rotor by considering the tunnel as a closed-loop structure with the train moving continuously inside at a constant speed. The initial study is carried with one end combined blade by placing the rotor 0.5 m away from the train. During solution initialization, the coefficient of torque,  $C_m$  shows a good starting torque with transient behavior predicting a positive peak torque coefficient of 0.99 during the acceleration period shown in Figure 8. The acceleration phase falls till  $t = 1.45$  s with a reasonable self-start by the rotor but this time delay will reduce the number of rotation of the rotor predicting less power generation. The rotor equilibrium period starts from  $t = 1.46$  s with an averaged peak torque coefficient,  $C_m$  of about 0.52 and predicted averaged, torque coefficient,  $C_m$  of 0.37. The time delay in self-start shows at minimum train speed the strength of the slipstreams boundary layers is quite weak that the rotor surface is not influenced by strong wind. These phenomena will change if the train speed is further increased. The rotor predicts a maximum  $C_p$  of 0.34 and an average  $C_p$  around 0.1.

The rotor self-starts slowly in the linear acceleration phase and then gradually attaining the plateau phase. The delay in self-start is well predicted from the time taken by the rotor to achieve steady rotational speed. The gradual increase in angular velocity also figures the loss in number rotation of the rotor attaining just  $\omega = 15.23$  rad/s at  $t = 12$  s seen in Figure 9. The present numerical study accurately predicts the acceleration phase and the converged plateau phase of the rotor in the considered time, which indicates the capability of the rotor to observe the flow after the self-start.<sup>18</sup> The rotational velocity of the rotor changes with different train speeds. Both the linear acceleration phase and the plateau phase of the rotor are accurately predicted. The rotor does not experience any equilibrium phase because the addition

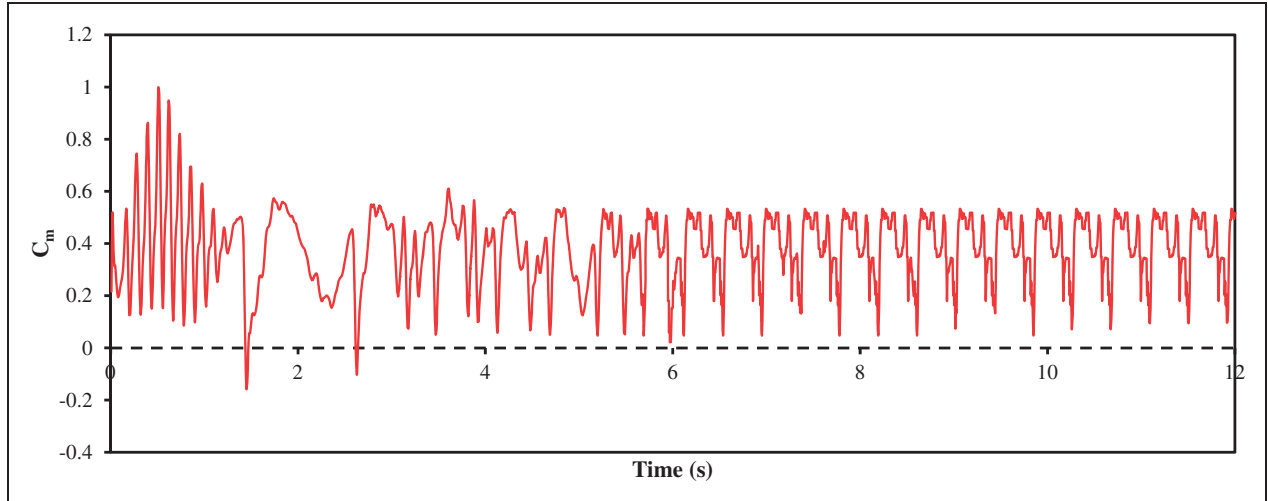


**Figure 8.** Torque coefficient with one end combined blades rotor at 6 m/s train speed.

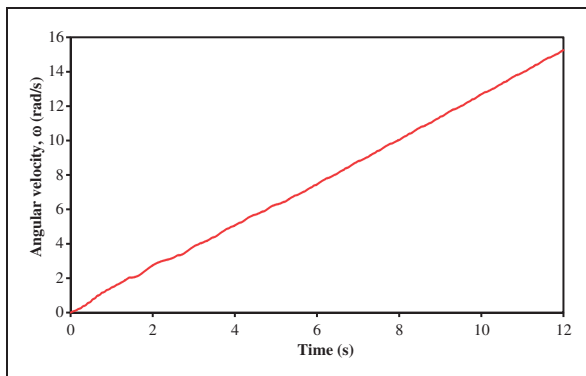


**Figure 9.** Passive rotational velocity of one end combined blades at 6 m/s train speed.

of opposing torque or the negative torque applied by the generator is neglected throughout the simulation only; the aerodynamic torque experienced by the rotor is calculated. The friction effect is neglected due to nonavailability of data in choosing the particular opposing torque.<sup>19</sup>

When the speed of the train is further increased to  $V_{\infty} = 12$  m/s there was a sudden shift in the coefficient of torque,  $C_m$  as the acceleration phase of the rotor got reduced and predicts the equilibrium phase at  $t = 0.7$  s much earlier than 6 m/s as shown in Figure 10. The reduced acceleration phase will directly increase the number of rotation of the rotor in the equilibrium phase. The rotor predicts a peak torque coefficient,  $C_m$  of 1.01 in the acceleration phase. While in the equilibrium phase, the averaged positive peak torque coefficient,  $C_m$  falls around 0.56 and the averaged torque coefficient,  $C_m$  was about 0.35. The rotor produces a maximum,  $C_p$  of 0.32 and averaged  $C_p$  of around 0.11. The rotational velocity of the rotor changes with different train speeds.

Again, the angular velocity versus time plot for  $V_{\infty} = 12$  m/s shows that the rotor predicts the linear acceleration phase earlier as the speed of the train is

increased. In Figure 11, a steady increase in the angular velocity is measured before achieving the plateau phase. The rotor gains a maximum angular velocity of about  $\omega = 28.78$  rad/s at  $t = 6$  s. Therefore, increase in the magnitude of slipstream regime between the tunnel and train does not affect the self-start of the rotor as the rotor clearly predicts the linear acceleration and stable equilibrium phase as shown in the plot.

At  $V_{\infty} = 18$  m/s the one end combined blades rotor's torque coefficient increases as the wave drag induced by the train to the rotor increases. The resultant moment of the rotor will increase, as the dragging flow on the concave side return blade will contribute to enhancing the torque. In the accelerating phase, the rotor predicts peak torque coefficient,  $C_m$  of about 1.05 presented in Figure 12.

Phenomenal increase in the torque coefficient,  $C_m$  of the rotor is observed as increase as the strength of the slipstream boundary increases attaining equilibrium phase very earlier at  $t = 0.47$  s. Later on, when settled the values become cyclic and stable. The averaged torque coefficient,  $C_m$  in the equilibrium phase falls for the train speed of  $V_{\infty} = 18$  m/s falls at 0.37 and the averaged positive peak torque coefficient,  $C_m$  falls around 0.6. Overall, as the strength of the slipstream boundary layer increases, the power obtained by the rotor drastically increases in  $t = 4$  s. Hence, the rotor predicts maximum  $C_p$  of 0.37 and averaged  $C_p$  around 0.12.

The increased wind gust along the train surface is sufficient to accelerate the rotor without any delay in the linear acceleration phase. The rotor attains the plateau region much earlier compared to the above-discussed different train speeds with an angular velocity of around 44 rad/s in  $t = 4$  s as shown in Figure 13. Formation of strong velocity gradient between the train surface and tunnel wall is developed due to the frictional force. Hence, the air around the train surface will be pushed along the train with the

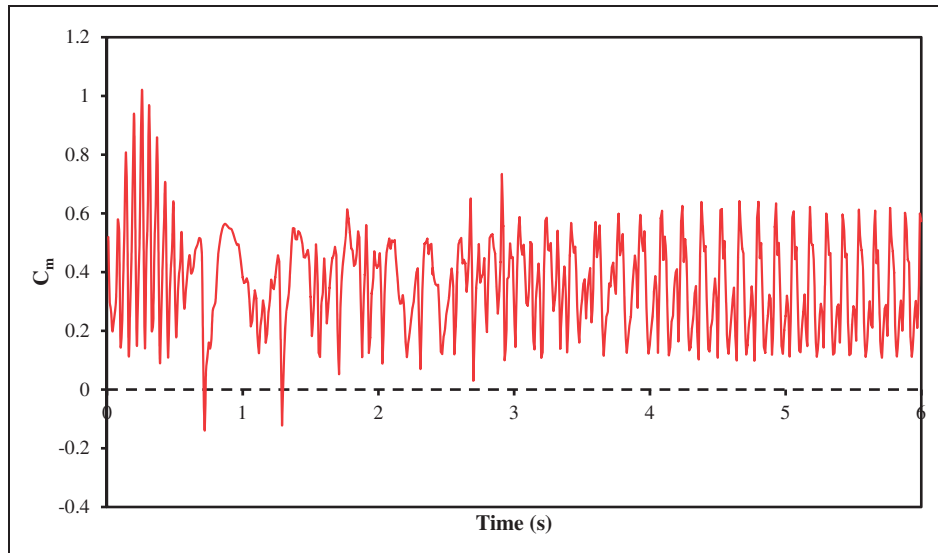


Figure 10. Torque coefficient with one end combined blades rotor at 12 m/s train speed.

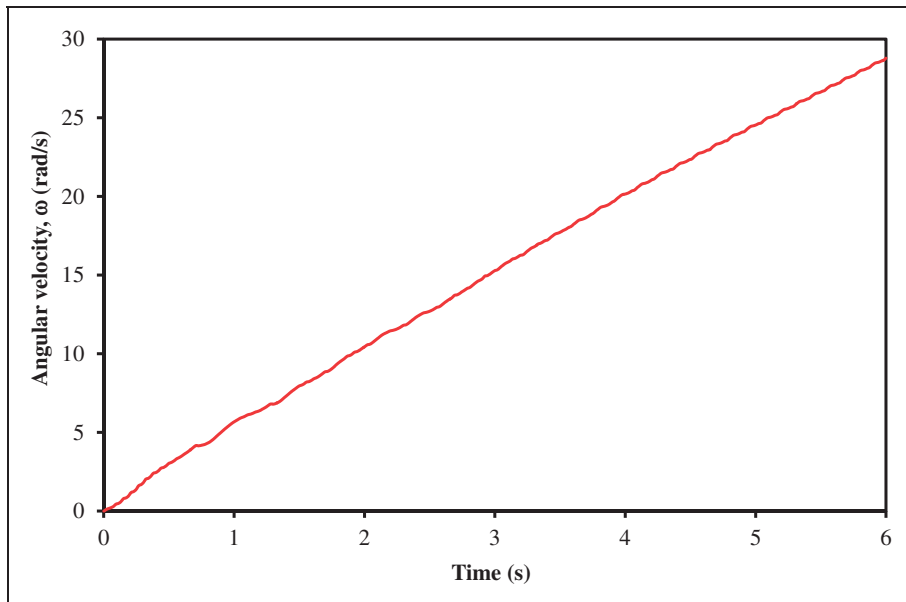


Figure 11. Passive rotational velocity of one end combined blades at 12 m/s train speed.

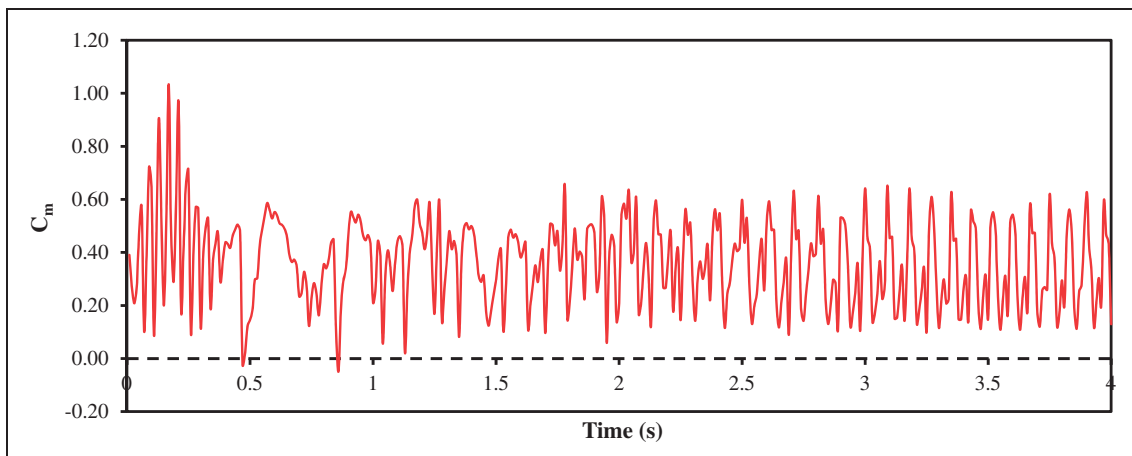
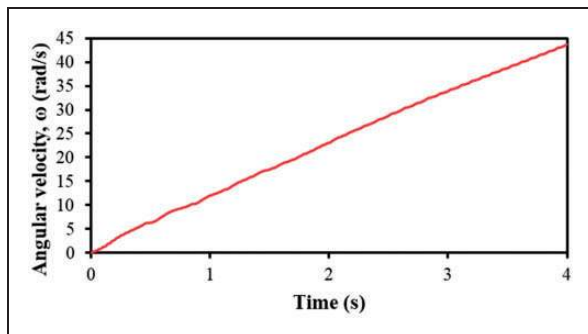


Figure 12. Torque coefficient with one end combined blades rotor at 18 m/s train speed.

speed of the train. At  $V_\infty = 18$  m/s there is no delay in self-start and the rotor achieves a steady passive rotational speed. The rotor gains a maximum angular velocity of 40.15 rad/s in the considered  $t = 4$  s.

**Rotor with both end combined blades.** The simulation for both combined blade shows a slight variation in the performance with that of the rotor with one end combined blade; for  $V_\infty = 6$  m/s the rotor predicts a peak torque coefficient,  $C_m$  in the accelerating period of 0.92. The rotor attains the equilibrium phase much earlier than that of the rotor with one end combined blade at  $t = 1.37$  s with all positive torque value for  $V_\infty = 6$  m/s. In the equilibrium phase, the rotor predicts an averaged peak torque coefficient,  $C_m$  of 0.6 and averaged torque coefficient,  $C_m$  of 0.4 as shown in Figure 14. In addition, the rotor predicts a maximum  $C_p$  of 0.36 and an average  $C_p$  around 0.12. The both end combined blades show significant performance than the one end combined blade in case of self-start and torque prediction. The elliptical shape in the concave side of the both end combined blades will increase the area of energy harvesting from the rotor center. The concave side of the blades is pushed by the deflected wind from the train gaining positive torque throughout the cycle. While the decrease in the distance at the convex side from the rotor center will



**Figure 13.** Passive rotational velocity of one end combined blades at 18 m/s train speed.

lead to negative torque in the returning blade with less obstacle energy. Therefore, the coefficient of drag on the convex side or blocking side is lesser than that of the concave side or advancing side of the rotor. Due to these phenomena, the performance of the both end combined blades is significantly compared with the one end combined blade.

The self-starting capability of the both end combined blades shows encouraging results for  $V_\infty = 6$  m/s; the linear acceleration phase is well predicted and the angular velocity steadily increases to attain plateau phase. Even at low train speed, the blades are able to hatch wind and self-start. At  $t = 12$  s the rotor attains a steady angular velocity of  $\omega = 15.65$  rad/s as indicated in Figure 15.

At train speed of  $V_\infty = 12$  m/s the both end combined blades show an excellent result in terms of torque predictions. The time taken to accelerate the rotor has been reduced which shows the rotor self-starts much earlier and attains equilibrium period quickly. At  $t = 0.47$  s the rotor starts the next cycle of operation with constant cyclic plot; this shows that the flow becomes realistic from the assumed condition. In the accelerating period, the rotor measures a positive peak torque,  $C_m$  of 1.03. Later on when the rotor becomes stable with averaged peak torque coefficient,  $C_m$  of 0.66 and an averaged torque coefficient,  $C_m$  of 0.39 as seen in Figure 16. In comparison with one end combined blades, the both end combined blades show significant variation in predicting the torque. The rotor predicts a maximum  $C_p$  of 0.54 and an average  $C_p$  around 0.16 in  $t = 6$  s.

The angular velocity plot predicts a steady rotational speed for  $V_\infty = 12$  m/s. From the graph, it is clearly visible that the initial linear acceleration of the turbine is well predicted. After the acceleration phase the passive rotational velocity of the turbine increases with time and almost linear after  $t = 2$  s reaching  $\omega = 31.32$  rad/s in the considered time presented in Figure 17.

In case of the maximum train speed  $V_\infty = 18$  m/s, during the solution initialization phase the rotor

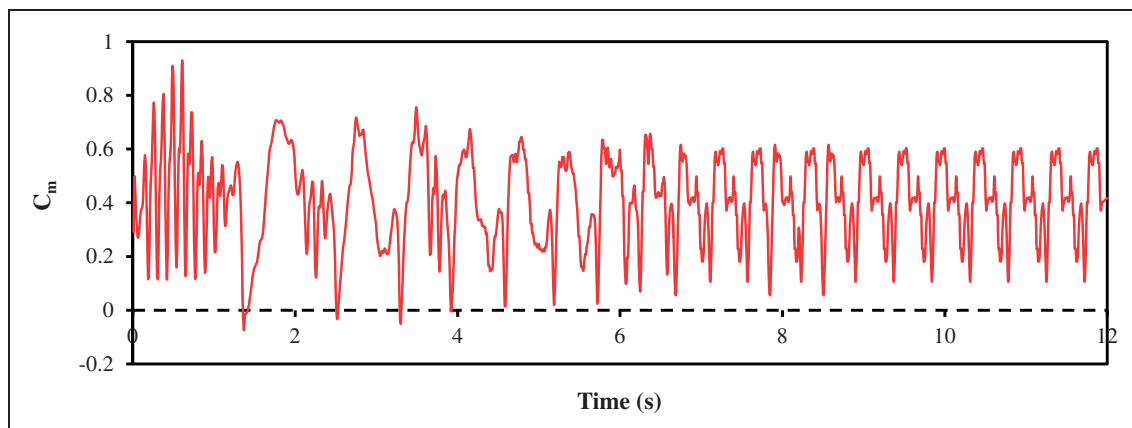


**Figure 14.** Torque coefficient with both end combined blades rotor at 6 m/s train speed.

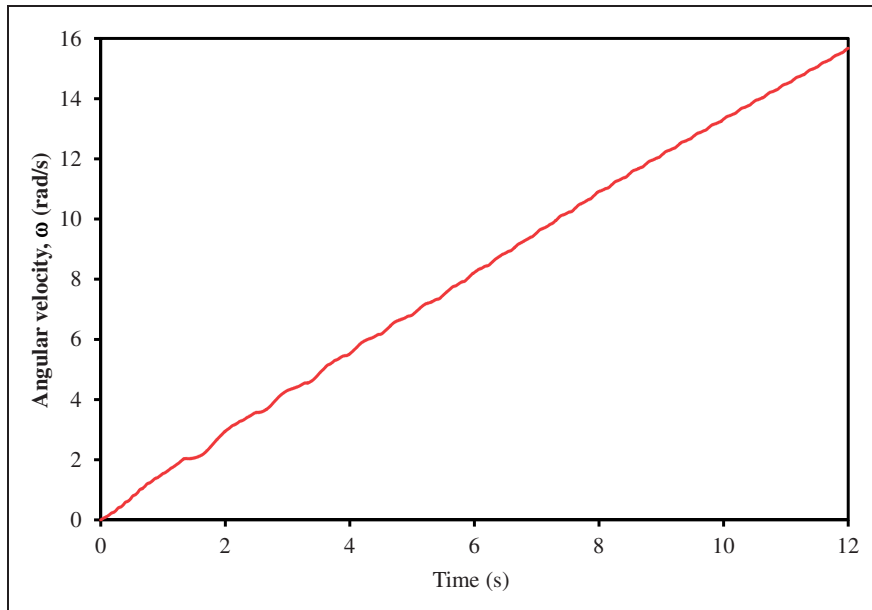


Figure 15. Passive rotational velocity of combined blades at 6 m/s train speed.

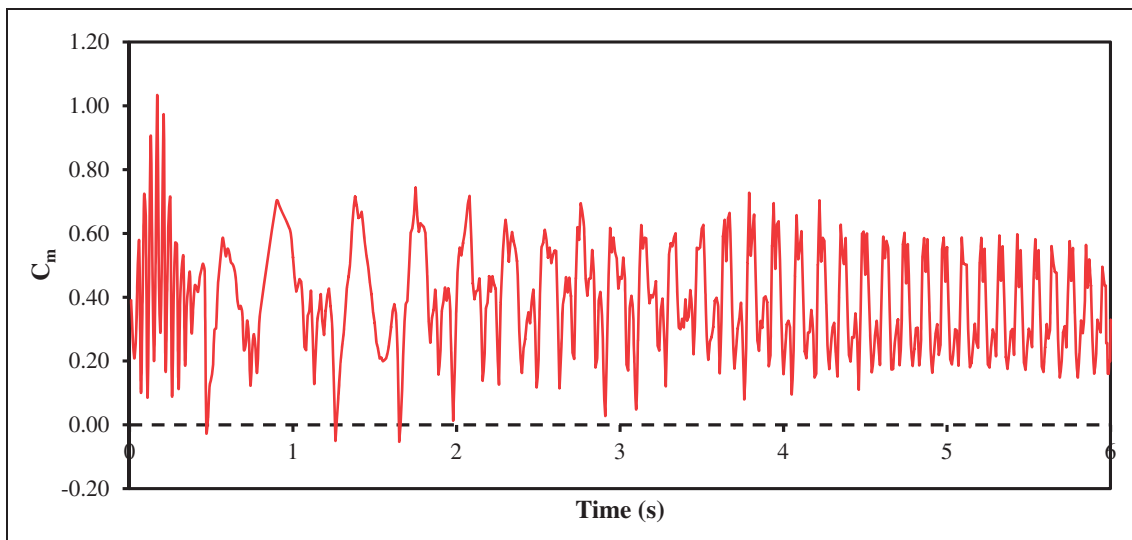


Figure 16. Torque coefficient with both end combined blades rotor at 12 m/s train speed.

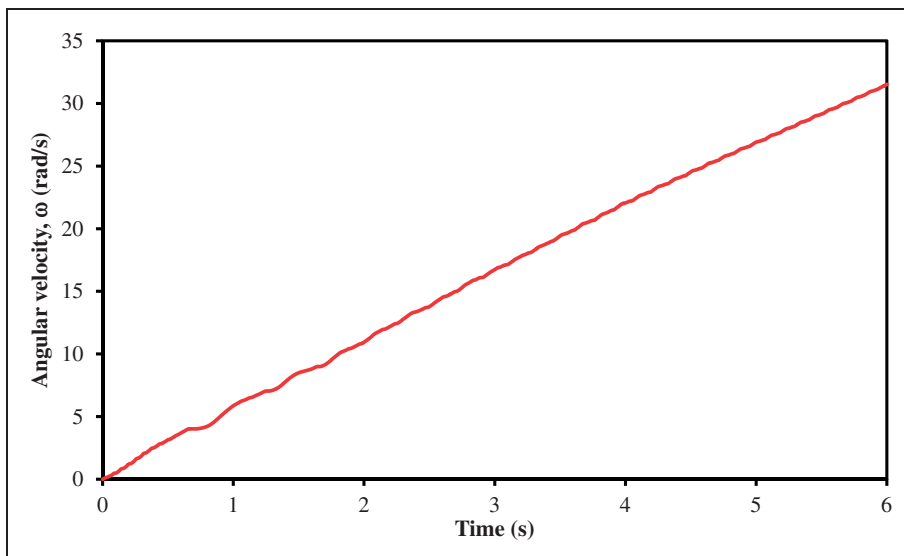


Figure 17. Passive rotational velocity of both end combined blades at 12 m/s train speed.

predicts two positive peak torque coefficient,  $C_m$  of around 0.82. Instability in predicting the torque occurs, as the assumed initial conditions may not be realistic but as the solution is converged, the torque coefficient becomes stable. The converged solution shows cyclic and realistic results with improved rotor number of rotation. Equilibrium period shows an averaged peak torque coefficient,  $C_m$  of 0.68 and averaged torque coefficient,  $C_m$  0.42. If the train travels with a maximum speed of  $V_\infty = 18$  m/s a single rotor placed along the length of the train is able to absorb a considerable amount of wind power in a considerable time of  $t = 4$  s as shown in Figure 18. The rotor measures maximum  $C_p$  around 0.45 and

averaged  $C_p$  around 0.14. Immense amount of power is predicted for a maximum train speed.

The passive rotational speed of the rotor increases drastically for  $V_\infty = 18$  m/s which is much predicted. The linear acceleration phase exists up to  $t = 0.4$  s defines the reduction in turbine self-start time. After  $t = 0.4$  s steady increase in angular velocity is predicted with  $\omega = 47.82$  rad/s at  $t = 4$  s as seen in Figure 19, which shows the rotor performance rely on the speed of the train in terms of acceleration and stable rotation.

Figure 20 shows a clear visualization of the frontal impact in the nose region of the train. The frontal impact makes acceleration of air along the train

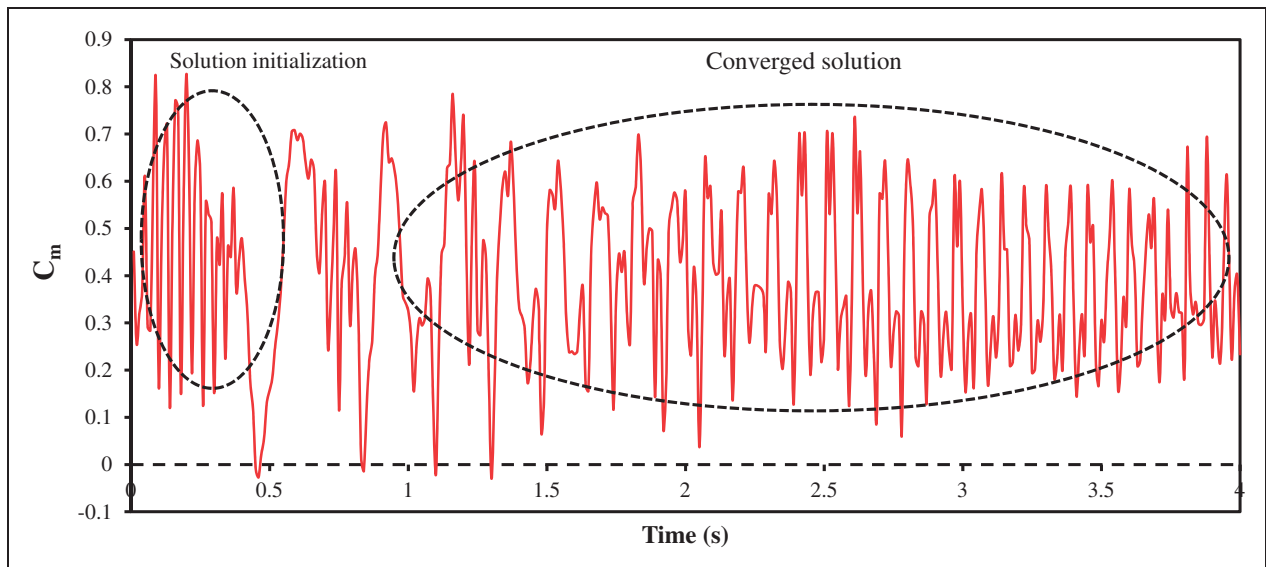


**Figure 18.** Torque coefficient with both end combined blades rotor at 18 m/s train speed.

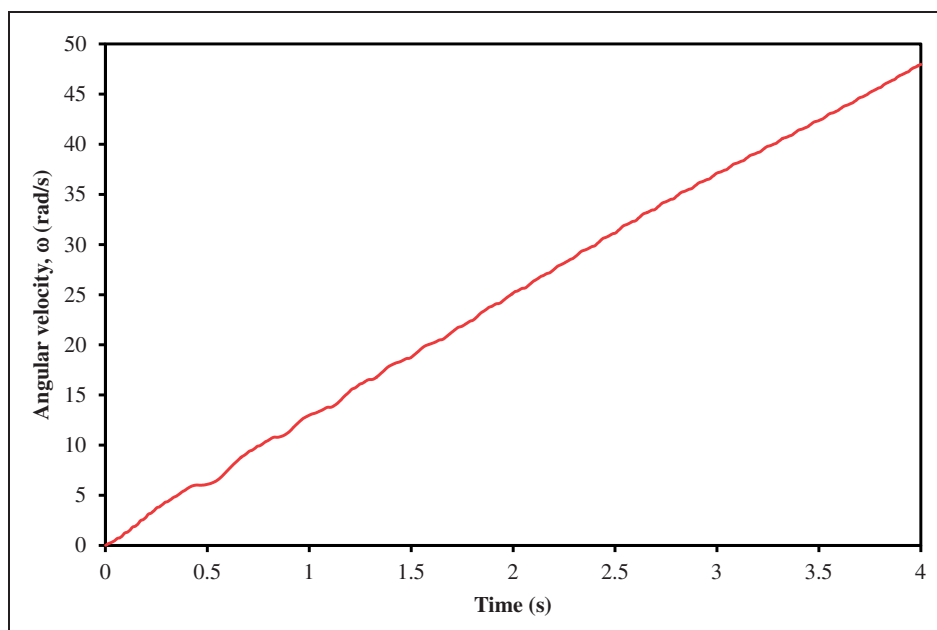


**Figure 19.** Passive rotational velocity of both end combined blades at 18 m/s train speed.

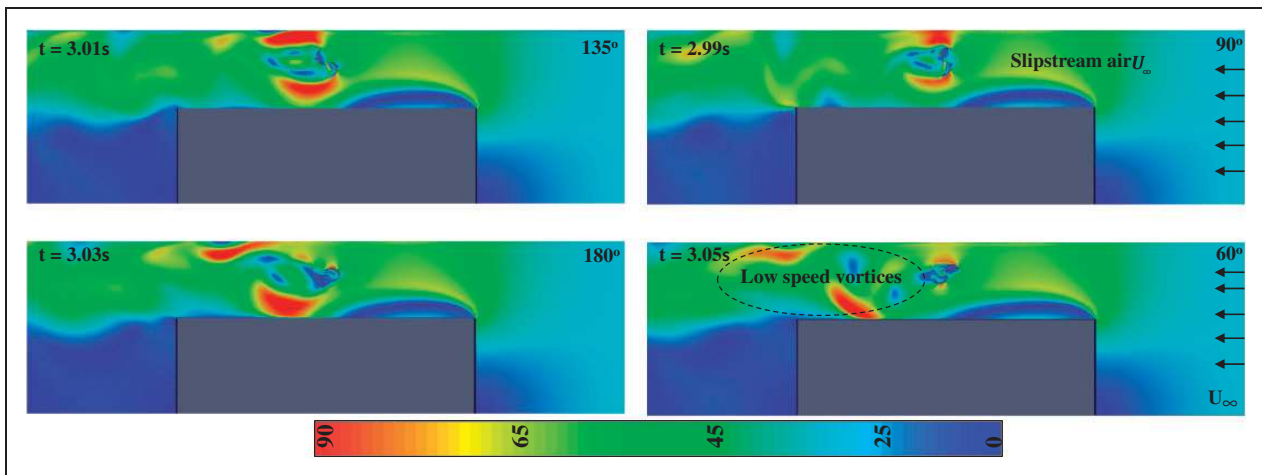


Figure 20. Contour of velocity field around both end combined blades at 18 m/s.

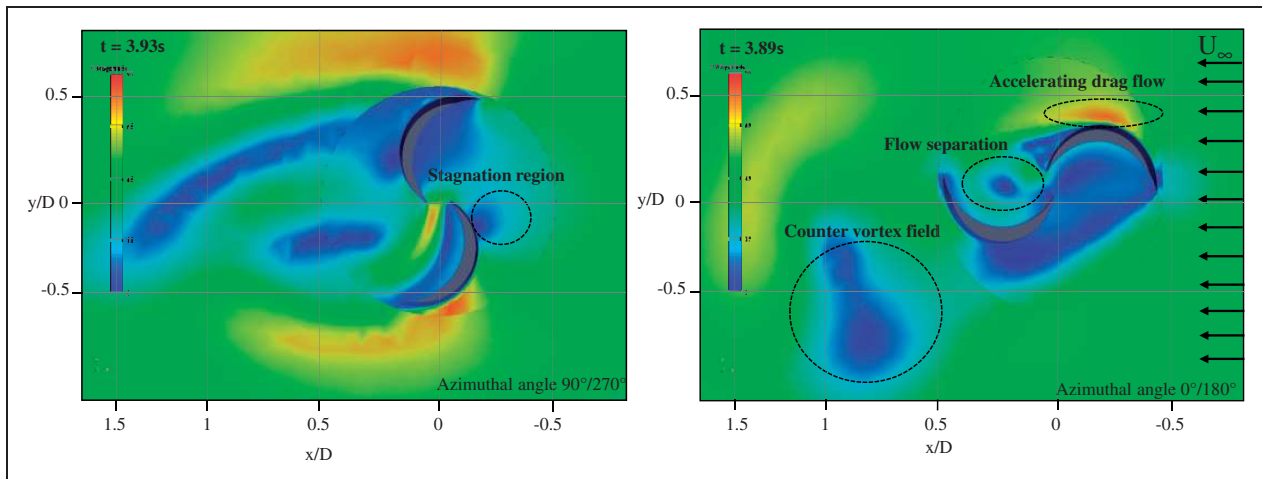


Figure 21. Variation in the velocity field on both end combined rotor with respect to time.

length forming slipstream boundary layer. The shear layer tends to form a recirculating bubble along the train surface that accelerates the flow further due to a reduced area between the tunnel and train. In addition, the speed of the train drags the surrounding air and increases the flow velocity. Due to viscosity, this increase in velocity contributes to the increase in the drag coefficient of the air along the train surface. The developed boundary layer zone has been visibly seen in the velocity contour plot. The developed slipstream velocity field between the train and the tunnel wall provides fruitful wind energy to the rotor. The wind velocity reduces from upstream to downstream once it hits the advancing blade of the rotor.

Flow acceleration is figured in the advancing blade convex side, which develops a lift force along the leeward side of the blade and the drag force on the windward side which self-starts the rotor (azimuthal angle  $0^\circ/180^\circ$ ) shown in Figure 21. Therefore, this acceleration on the leeward side of the blade leads to flow separation. The evolution of higher velocity distribution at the rotor blade ends suggests

the blades develop a considerable amount of torque. When the rotor is at the azimuthal angle ( $90^\circ/270^\circ$ ) the pressure side of the advancing blade experiences a higher stagnation of flow than the returning blade results in continuous rotor rotation. Only the counter vortex field shed from the blade tip reduces the rotor performance creating a wake region behind the rotor.

From the pressure contour of the both end combined blades it is observed that how pressure variation occurs from upstream to downstream of the rotor. This variation in pressure shows the rotor extraction of wind power from the developed slipstream boundary layer field. When the train nose makes an impact with the air a sudden strong head pressure pulse is formed in front of the nose region; this sudden jump in pressure changes the surrounding pressure inside the tunnel as shown in Figure 22. A varying pressure in the boundary layer region of the slipstream creates drag waves that are absorbed by the rotor. Therefore, the advancing blade experiences a high pressure along the concave surface of the blade to develop a positive

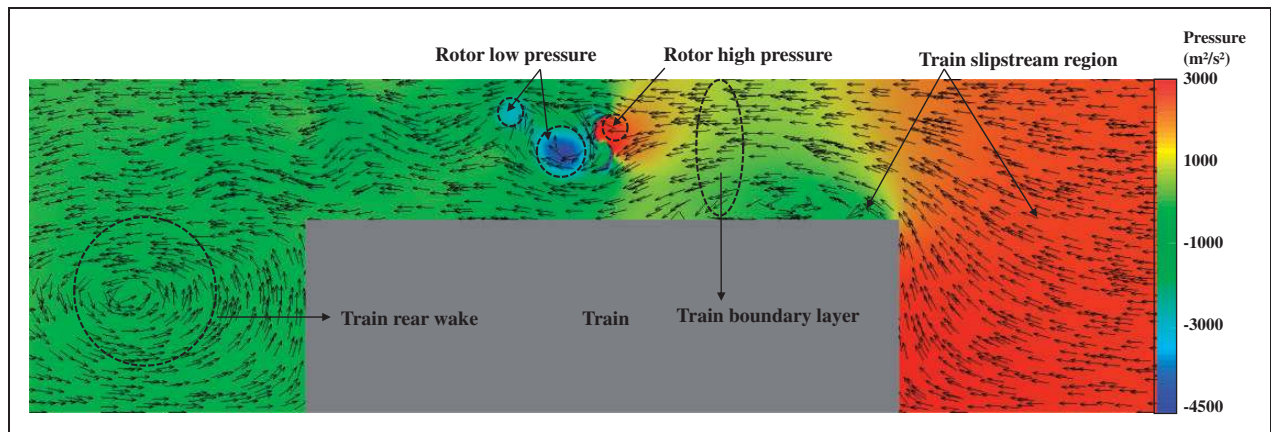


**Figure 22.** Contour of pressure field around both end combined blades at 18 m/s.

torque. The positive torque is continuously supplied from the sheared airflow while the low-pressure vortex formation along the convex side of the blade reduces torque. Hence from the pressure contour, relatively high pressure on the concave side of the rotor gives rise to increased positive torque or power output,<sup>20</sup> whereas returning blade is not much affected by low pressure with only two low pressure vortices so the negative torque will not affect much of the power production.

## Conclusion

Some conclusions on the study of power extraction from a speeding train with two different blade models using OpenFOAM®:

- Both the modified rotors are able to harvest wind energy from the slipstream developed by the speeding train. The blades predict a remarkable torque coefficient with respect to the different train speeds. The slipstream boundary layer regime is carefully modeled around the train and torque is measured.
- The both end combined blades show better performance in terms of predicting the torque coefficient. A considerable increase in torque coefficient is due to the elliptical shape in the concave side of both end combined blades which contributes to an increase in the energy harnessing distance from the rotor origin. In addition, the construction of both the combined and one end combined blades remains simple as that of conventional Savonius wind rotor.
- The both end combined blades are able to harvest the high shear slipstream of wind along the concave side of the blade. The flow acceleration on convex side of the both end combined blade is on the higher note, which helps to generate lift and reduces the delay in self-starting. So if we consider three-dimensional modeling of the rotor then considerable amount of wind energy can be harnessed.

## Declaration of Conflicting Interests

The author(s) declared no potential conflicts of interest with respect to the research, authorship, and/or publication of this article.

## Funding

The author(s) disclosed receipt of the following financial support for the research, authorship, and/or publication of this article: Institute of High Performance Computing, A\*STAR in Singapore has supported this research.

## ORCID iD

Praveen Laws  <http://orcid.org/0000-0002-2114-2257>.

## References

1. Ahmed SR, Gawthorpe RG and Mackrodt PA. Aerodynamics of road and rail vehicles. *Veh Syst Dyn* 1985; 14: 319–392.
2. Lee HH. *Assessment of potential aerodynamic effects on personnel and equipment in proximity to high-speed train operations*. US Department of Transportation Federal Railroad Administration, No. DOT/FRA/ORD-99/11; Washington, D.C, 1999.
3. Raczkowski R. Road sheltering and optimization. Patent application 12/948807, USA, 2011.
4. Chen T. *Power generation system utilizing wind draft from vehicular traffic*. Patent 7427173, USA, 2008.
5. Hyeon RC, Cho S and Hye HS. Wind tunnel concept converts wind energy generated by subway trains into electricity, <https://www.greenoptimistic.com/wind-tunnel-concept-20100906/#.WtY6f4huaUk> (2010, accessed 13 March 2017).
6. Jiang Q and Luparini AL. T-box wind power generator report, <http://www.coroflot.com/JQ/T-BOX> (2011, accessed 25 December 2014).
7. Khadka N. *Efficient use of wind energy to generate electrical power by means of wind tunnel effect and Coanda effect*. Bachelor Thesis, School of Electrical and Electronic Engineering, Charles Darwin University, Australia, 2015.
8. Sanusi A, Soeparman S and Wahyudi S. Experimental study of combined blade Savonius wind turbine. *Int J Renew Energy Res* 2016; 6: 614–619.

9. Rangappa R, Vathumalai S and Chung E. CFD analysis on wind flow characteristics while a train passing through the tunnel. *Int J Adv Mech Civ Eng* 2015; 51–54.
10. Niu J, Zhou D and Liang X. Numerical study on the aerodynamic pressure of a metro train running between two adjacent platforms. *Tunnel Underground Space Technol* 2017; 65: 187–199.
11. Trains SG. Alstom metropolis C830, <http://www.sgtrains.com/train-c830.html> (2017, accessed 20 June 2017).
12. Tian W, Song B and VanZwieten JH. Computational fluid dynamics prediction of a modified Savonius wind turbine with novel blade shapes. *Energies* 2015; 8: 7915–7929.
13. Greenshields C. OpenFOAM 2.3.0: Arbitrary mesh interface, <https://openfoam.org/release/2-3-0/non-conforming-ami/> (2011, accessed 17 February 2014).
14. OpenFOAMWiki. PimpleDyMFoam, <http://openfoamwiki.net/index.php/PimpleDyMFoam> (2014, accessed 15 May 2014).
15. Devolder B, Schmitt P and Rauwoens P. A review of the implicit motion solver algorithm in OpenFOAM® to simulate a heaving buoy. In: *NUTTS conference 2015: 18th numerical towing tank symposium*, 2015, pp.1–6. Marstrand, Sweden: Curran Associates, Inc.
16. Hemida H, Baker C and Gao G. The calculation of train slipstreams using large-eddy simulation. *Proc IMechE, Part F: J Rail and Rapid Transit* 2014; 228: 25–36.
17. Kuron M. 3 criteria for assessing CFD convergence, <https://www.engineering.com/DesignSoftware/DesignSoftwareArticles/ArticleID/9296/3-Criteria-for-Assessing-CFD-Convergence.aspx> (2015, accessed 6 January 2015).
18. Zhu J, Huang H and Shen H. Self-starting aerodynamics analysis of vertical axis wind turbine. *Adv Mech Eng* 2015; 7: 1–12.
19. Hill N, Dominy R, Ingram G, et al. Darrieus turbines: the physics of self-starting. *Proc IMechE, Part A: J Power and Energy* 2009; 223: 21–29.
20. Zhou T and Rempfer D. Numerical study of detailed flow field and performance of Savonius wind turbines. *Renew Energy* 2013; 51: 373–381.